Prediction of impedance characteristic during electrical stimulation with microelectrode arrays

Journal of Neural Engineering

PAPER

Prediction of impedance characteristic during electrical stimulation with microelectrode arrays

Andreas Erbslöh[1,7,*], **Julius Zimmermann**[2,7,*], **Sven Ingebrandt**[4], **Wilfried Mokwa**[4], **Karsten Seidl**[3], **Ursula van Rienen**[2,5,6], **Gregor Schiele**[1] and **Rainer Kokozinski**[3]

[1] Intelligent Embedded Systems Lab, University of Duisburg-Essen, Duisburg, Germany
[2] Institute of General Electrical Engineering, University of Rostock, Rostock, Germany
[3] Department of Electronic Components and Circuits, University of Duisburg-Essen, Duisburg, Germany
[4] Institute of Materials in Electrical Engineering 1, RWTH Aachen, Aachen, Germany
[5] Department Life, Light and Matter, University of Rostock, Rostock, Germany
[6] Department of Ageing of Individuals and Society, University of Rostock, Rostock, Germany
[7] These authors contributed equally.
[*] Authors to whom any correspondence should be addressed.

E-mail: andreas.erbsloeh@uni-due.de, julius.zimmermann@uni-rostock.de and ursula.van-rienen@uni-rostock.de

Keywords: microelectrode array, electrical impedance spectroscopy, electrode-electrolyte interface, functional electrical stimulation, impedance measurement

OPEN ACCESS

RECEIVED
28 August 2024

REVISED
20 January 2025

ACCEPTED FOR PUBLICATION
19 March 2025

PUBLISHED
11 April 2025

Abstract

Objective. Modern neural devices allow to interact with degenerated tissue in order to restore sensoric loss function and to suppress symptoms of neurodegenerative diseases using microelectronic arrays (MEA). They have a bidirectional interface for performing electrical stimulation to write-in new information and for recording the neural activity to read-out a neural task, e.g. movement ambitions. For both applications, the electrical impedance of the electrode-tissue interface (ETI) is crucial. However, the ETI can change during run-time due to encapsulation effects and changes of the neuronal structures. We investigated if an impedance spectrum can be reliably extracted from recordings during stimulation with microelectrode arrays. *Approach.* We present a measurement method for characterizing the electrical impedance spectrum during stimulation. We performed charge-controlled stimulation with a penetrating microelectrode array in an electrolyte solution. From the stimulation recordings, we extracted the impedance. Furthermore, a numerical model (digital twin) of the stimulation electrodes is established. *Main results.* We obtained consistent results for relevant electrochemical using electrochemical impedance spectroscopy, time-domain analysis and Fourier-transform-based impedance estimation. Moreover, the numerical simulations confirmed that the measured microelectrode had the expected properties. *Significance.* Our results pave the way to enable a live assessment of the impedance in future MEA-based neural devices. This will enable adaptive electrical stimulation or (re-)selection of recording electrodes by taking the actual state of the electrode into account.

1. Introduction

Neurodegenerative diseases like Retinopathia Pigmentosa (visual degeneration) [24] or Morbus Parkinson (movement disorder) [25] and injuries of the nervous system [20] result in a reduction or progressive loss of sensory or motor functionalities in patients. Electrical stimulation is used to write-in new information to alleviate symptoms as for example in deep brain stimulation (DBS) [12], retinal [15] or cochlear implants [4]. In the case of DBS, the electrical stimulation overrides neuronal activity to suppress Parkinson motor symptoms [12, 28]. While established clinical routines for electrical stimulation exist, more research is required to increase the effectiveness and patient-friendly use of these devices in new therapies [15]. An important aspect for the next generations of neural implants, brain–computer

interfaces or stimulation electrodes is to enable not only the write-in of information but also the read-out [9].

In this regard, adaptive stimulation or closed-loop stimulation promises to achieve a long-term reliability of neural devices. The main idea is that the stimulation parameter will be adapted during run-time by considering the tissue behaviour from neural recordings and tissue encoding [32] and by considering impedance properties due to an internal measurement unit. These systems allow to recover the stimulation efficiency in a patient if the tissue changes due to neurodegenerative degeneration. Devices with such functionality have a bidirectional front-end for simultaneously enabling electrical stimulation and recording the neural activity [27]. Thanks to their small size and large number of active channels, microelectrode arrays have become popular. They enable, among others, a spatial specificity, which is in particular relevant for retinal implants [15]. However, a major challenge is the electrode-tissue interface (ETI). Its impedance affects both stimulation [3] and recording [19].

The interface impedance usually changes after implantation over time due to the material-tissue interaction [38]. The strength of the interaction depends on the level of the body reaction [18] and of the electrochemically induced degradation of the electrode material [13, 23] or through the impact of electrical stimulation [21]. As a result, the effectiveness of the neuronal devices weakens over time because the stimulation effect decreases and the sensing property for neural recording quality is reduced. A possible intervention to stabilise the treatment effect is to tune the stimulation parameters, which can lead to further adversarial effects.

Before implantation, the impedance spectrum of electrode arrays is commonly measured over a wide frequency range (e.g. from the Hz to MHz range) by electrical impedance spectroscopy (EIS) to assess the performance of the neural interface [2]. EIS measurements over a broad frequency range have the disadvantage of a relatively long measurement time and may require special hardware to resolve the impedance at various orders of magnitude, which can occur for example due to capacitive behaviour at low frequencies. Thus, EIS of implanted electrodes can be straightforwardly conducted only immediately after implantation and before explantation. Instead, the impedance magnitude at only one frequency (mostly at 1 kHz) is measured during chronic stimulation [10, 16, 19, 29, 33, 36]. Measuring at one frequency is much faster than recording an entire spectrum but yields a low information gain. For example, recording the impedance magnitude at 1 kHz in rodents motor cortex over six months [36] has revealed a 100–400 times increased impedance at 1 kHz during the first six weeks after implantation, which afterwards decreased back to the initial value. Modern recording probes such as the NeuroPixel 2.0 have proven to enable stable recording quality an even longer period of 309 days [35]. However, without measuring the impedance at multiple frequencies, the observed impedance change cannot be clearly attributed to a particular process (e.g. changes of the electrochemical interface or biological processes such as scarring).

Using the information of the impedance spectrum in particular frequency bands can be used to disentangle, for example, electrochemical reactions or changes in the tissue [41]. Thus, a detailed understanding of the individual impedances contributing to the total impedance becomes feasible with recordings covering a wide frequency spectrum [18, 21, 23].

For that, ways to estimate the impedance spectrum using the response signals from the electrical stimulation are required to circumvent the need for special equipment for EIS recordings. Another relevant aspect is that EIS is conducted at low voltage or current amplitudes to avoid nonlinear effects while the stimulation amplitudes may be considerably higher [26]. Thus, estimating the impedance directly from the stimulation pulses permits to identify nonlinear effects and corresponding electrochemical reactions as revealed by previous investigations on macroscopic Platinum electrodes [1, 42].

Characterising the impedance during the implantation offers several advantages for neural devices with multielectrode stimulation and recording front-ends. For example, the strength of the ETI impedance can be tracked during run-time. Ideally, also the local tissue conductance can be inferred by disentangling the ETI and tissue impedances. Hence, the right channel for electrical stimulation with a low impedance and thus low energy requirements can be chosen. In addition, defect channels can be detected and the stimulation and recording front-end can be disabled. This approach would thus be relevant for multiple applications ranging from DBS to retinal or cochlear implants.

In this work, we present a method that allows to characterize the electrical impedance behavior by processing the recorded transients of input voltage and current. Figure 1 shows a black-box model for processing the transient current injection $I_{\mathrm{elec}}(t)$ and the different electrode voltage $\Delta U_{\mathrm{elec}}(t)$ in order to extract the parameters of the corresponding impedance model. For this, we have applied the charge-controlled stimulation (ChCS) method using microelectrode arrays in electrolyte solution.

This paper is structured into three main parts: First, the used microelectronic array (MEA), its electrochemical characterisation and the ChCS method are described. Then, we introduce a measurement method for extracting the resistive and capacitive load of the stimulation front-end by using the transient current and voltage input. Finally, we explore a method for extracting the impedance properties of

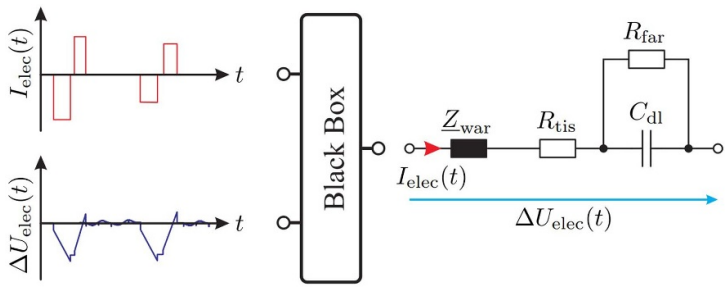

Figure 1. Blackbox model for processing transient signals of the electrical stimulation to extract the parameters of the Randles model which describe the electrolyte and tissue part between the working and counter electrode (circuit elements: Warburg impedance Z_{war}, tissue resistance R_{tis}, double-layer capacity C_{dl}, Faraday resistance R_{far}).

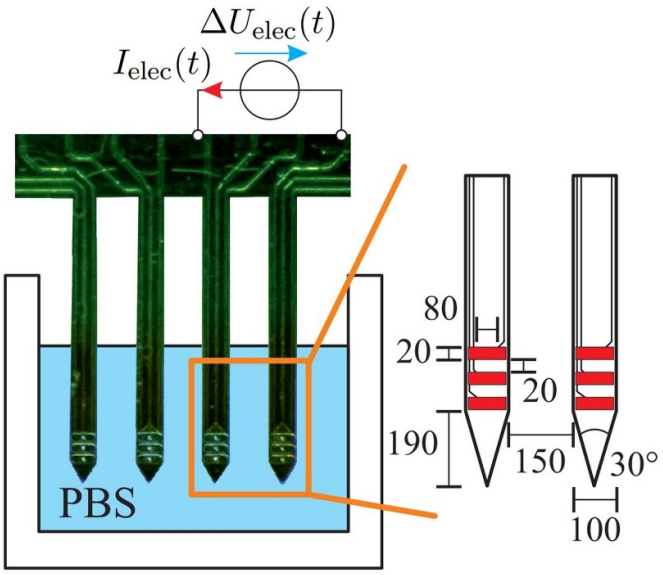

Figure 2. Top view of the used microelectrode array (planned for depth-wise stimulation and recording of the retina) which is conducted in phosphate-buffered saline (PBS) solvent in order to perform electrical stimulation and extract the electrical model parameters.

the ETI from the transient current and voltage input. We discuss how this method can be implemented on real hardware and introduce a link to numerical simulations, which paves the way towards a digital twin that enables continuous, location-specific monitoring and control of the stimulation.

2. Methods

2.1. Layout of the microelectrode arrays

Figure 2 shows the experimental setup in which the active area of the MEA is immersed in a phosphate-buffered saline (PBS). The MEAs were designed and fabricated at the Institute of Materials in Electrical Engineering 1 (IWE1, RWTH Aachen). They have been used for investigating closed loop retinal stimulation with deep-selective stimulation and recording capability [27].

The MEAs have four shafts. Each shaft has three Iridium oxide (IrOx) electrodes with a square area A_{el} of 1600 μm^2 (80 $\times$ 20 μm^2). The distance between the electrodes on a shank is 20 μm in order to get access to the retinal ganglion, bipolar and amacrine cells. Each shank has a length of 1 mm and the distance between each shank is 150 μm. The tips of the shafts have an angle of 30° to facilitate insertion into the tissue [27]. During fabrication, the electrode material is sputtered on a silicon substrate and the structure of the probes is etched into the substrate. The probes are released by using a thinning process after the clean room fabrication.

2.2. Electrochemical characterisation

After the fabrication process, the electrodes of the MEA were characterised by EIS in PBS at room temperature (300 K).

For measuring the impedance, we used a two-electrodes setup with both electrodes being local MEA electrodes. The results are shown in figure 5, in which the sweep was done for a frequency range of 1 Hz and 1 MHz with a peak voltage of 20 mV and a point repetition of 30.

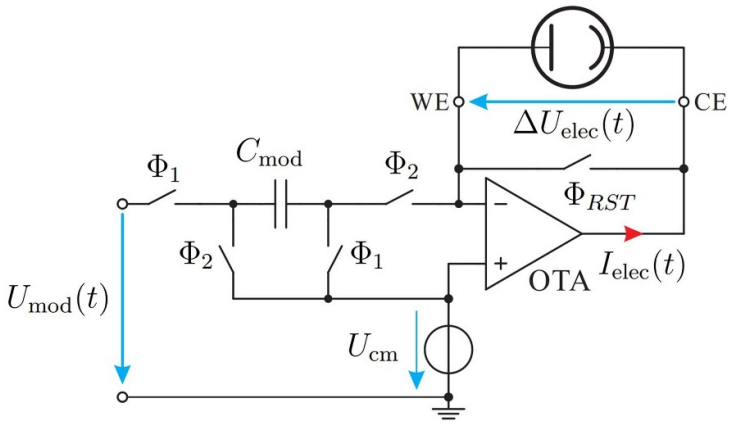

Figure 3. Circuit schematic of the charge-controlled stimulation front-end in which the impact of the stimulation path is implemented in the feedback.

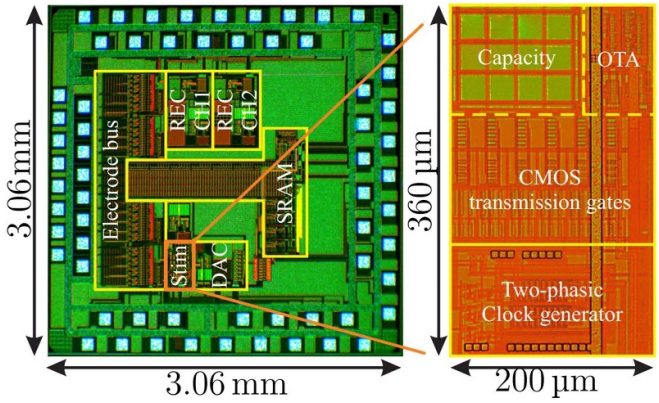

Figure 4. Layout of the fabricated ASIC with the presented charge controlled stimulator for high-accuracy applications.

2.3. ChCS front-end

Compared to voltage-controlled stimulation (VCS) and current-controlled stimulation (CCS), ChCS enables a high-frequency charge transfer, which combines a high energy efficiency by controlling the injected charge with clocks [34]. VCS is highly energy-efficient but it needs more hardware resources and the injected charge amount is not known without an additional measurement circuit. CCS in principle permits to control the injected charge amount but uncertaincy arises due to clock feedthrough.

The charge transfer in ChCS takes place with a high number of clock cycles. In each clock cycle a small charge packet will be generated on the modulator side (end of phase Φ_1) and transferred to the metal-tissue-interface (end of Φ_2). This enables a stimulation scheme which combines the advantages of VCS and CCS in order to achieve long-term stable stimulation.

Figure 3 shows the CMOS circuit of the active feedback ChCS modulator by using a switched capacitor (SC) integrator with the corresponding realisation in figure 4. To achieve a high gain and a high output resistance, a cascaded current-mirror OTA topology was selected for the SC integrator.

The double-layer capacitance of the electrode interface is used as load capacitance. While implementations without any feedback structure of the ChCS with a SC-emulated resistance have been described [14, 17], it has been shown that these implementations cannot be used with microelectrodes [8].

The charge amount during each charge transfer is highly controllable due to the switched-capacitor principle. Each charge transfer causes an exponentially decreasing current pulse (1) with the tissue-dependent time constant τ_{RC} (2)

$$I_{\mathrm{elec}}(t) = \frac{U_{\mathrm{in}}(t)}{R_{\mathrm{tis}}||R_{\mathrm{far}}} \cdot \exp\left(-\frac{t}{\tau_{\mathrm{RC}}}\right) \quad (1)$$

$$\tau_{\mathrm{RC}} = (R_{\mathrm{tis}}||R_{\mathrm{far}}) \cdot (C_{\mathrm{dl}}||C_{\mathrm{mod}}) \approx R_{\mathrm{tis}} \cdot C_{\mathrm{mod}} \quad (2)$$

$$Q_{\mathrm{mod}} = C_{\mathrm{mod}}\, U_{\mathrm{mod}} \cdot \underbrace{\left[1 - \exp\left(-\frac{2}{f_{\mathrm{mod}}\, \tau_{\mathrm{RC}}}\right)\right]}_{\approx 1} \quad (3)$$

$$Q_{\mathrm{inj,cat}} = \int_0^{T_{\mathrm{cat}}} I_{\mathrm{EL}}(t)\, \mathrm{d}t = \underbrace{T_{\mathrm{cat}}\, f_{\mathrm{mod}}}_{n_{\mathrm{cat}}}\, Q_{\mathrm{mod}}. \quad (4)$$

With the time integration over the active duration of a modulator clock f_{mod}, (3) yields the amount of charge transferred for each charge transfer Q_{mod}, which depends on the used modulator voltage U_{mod} and the modulator capacity C_{mod}. The total injected charge amount for the cathodic phase $Q_{inj,cat}$ can be calculated using (4) and depends on the number of injected charge transfers n_{cat}. This is a product of the chosen modulator frequency f_{mod} and the cathodic phase duration T_{cat}. For this setup, a fixed C_{mod} of 10 pF was chosen and hence a maximum modulator voltage of 1.6 V is available to generate up to 18.56 pC in each clock. The maximum modulator clock depends on the time constant τ_{RC} which is dominantly impacted by the tissue resistance.

2.4. Stimulation protocol

The working principle of the ChCS frontend was tested with a stimulation protocol in 0.9% PBS with the MEA structures. Before and after the stimulation session, EIS was performed. For measuring the transient signals from the electrical stimulation, the injected current I_{elec} and corresponding voltage difference ΔU_{elec} were captured with the mixed-signal digital oscilloscope MDO-3034 from Tektronix at a sampling rate of 25 MSPS and a 10-bit resolution. The injected current was sensed with a custom-made measurement board featuring a circuit of a high-speed shunt-resistive instrumentation amplifier. The board also captured the differential voltage between two selected electrode channels.

The ChCS front-end was controlled via an embedded setup and the settings were prepared in an additional LabVIEW interface. To determine the functionality of the ChCS modulator, the phase duration T_{ph} was swept from 400 μs to 20 ms in 10 steps. Each step was repeated 50 times. A biphasic rectangular pattern with an interphase duration of 10% of the active phase duration was chosen. The injected charge amount is in all settings at $-4\,\text{nC} \cdot \frac{T_{ph}}{20\,\text{ms}}$ by adapting the modulator frequency f_{mod} and the modulator voltage U_{mod}. The corresponding parameter extraction was done with an offline data processing in MATLAB.

2.5. Numerical model

The microelectrode array, with the structure in figure 2, is modelled in the FEM modelling software NGSolve [30], which uses the OpenCascade CAD kernel[8] and is built on the mesh generator NETGEN [31]. The electrode arrays were immersed in a homogeneous medium to model the PBS environment during electrochemical characterisation experiments. Dirichlet boundary conditions were applied on the active contacts according to the experiment and the impedance was computed (for more details, see [42]). As PBS is resistive at the considered frequencies, only the PBS conductivity was considered and the expected resistance was computed, which should agree with the measured tissue resistance R_{tis} (see equation (5)). The numerical model of the electrode predicts the pure electrode impedance (i.e. without an electrochemical interface) [42].

[8] www.opencascade.com/.

3. Results and discussion

3.1. Electrochemical characterisation of the microelectrode arrays

The impedance magnitude and phase had a characteristic shape (figure 5). The phase of the impedance increases from $-55°$ at 1 Hz to 0° at 355 kHz, which highlights the transition from capacitive to resistive behaviour. At a frequency of 1 kHz, an absolute impedance of about 54 kΩ was measured.

To gain more insight from the EIS characterisation, we considered the Randles circuit (see also figure 1), whose impedance is described by

$$\underline{Z}_{elec}(\omega) = R_{tis} + \frac{R_{ct}}{1 + j\omega R_{ct} C_{dl}} + \frac{\overbrace{\sigma_w}^{=\underline{Z}_{war}(\omega)}}{(j\omega)^{1/2}}. \quad (5)$$

The impedance of the Randles model $\underline{Z}_{elec}$ comprises a tissue resistance R_{tis}, a faradaic charge deposition of the double layer interface C_{dl}, the charge-transfer resistance R_{ct}, and the Warburg impedance $\underline{Z}_{war}$ comprising the Warburg coefficient σ_w.

The parameter fit yielded a tissue resistance R_{tis} of 9.9 kΩ, a double layer capacity C_{dl} of 113.4 nF, a charge-transfer resistance R_{ct} of 2.2 MΩ, and the Warburg coefficient of σ_w of 2.5 $\text{MΩ/Hz}^{-0.5}$.

3.2. Estimation of resistive and capacitive stimulation load

We devised a method to extract parameters of a simple stimulation load. This method uses the change in voltage during the active charge transfer in order to estimate the resistance and capacitive load during stimulation. During stimulation, the corresponding voltage waveform ΔU_{elec} is related to the injected current I_{elec} and the electrical properties of the Randles model of the metal-electrode interface within the stimulation path as described by (6). Here, a simplified version of the Randles model is used in which the tissue resistance R_{tis} and double-layer capacitance C_{dl} are connected in series

$$\Delta U_{elec}(t) = I_{elec}(t) \cdot R_{tis} + \frac{1}{C_{dl}} \int I_{elec}(t)\, \mathrm{d}t. \quad (6)$$

Figure 6 shows the measurement results of the transient stimulation signals with an additional zoom into the anodic phase (time-window of 100 μs) from the anodic-first stimulation.

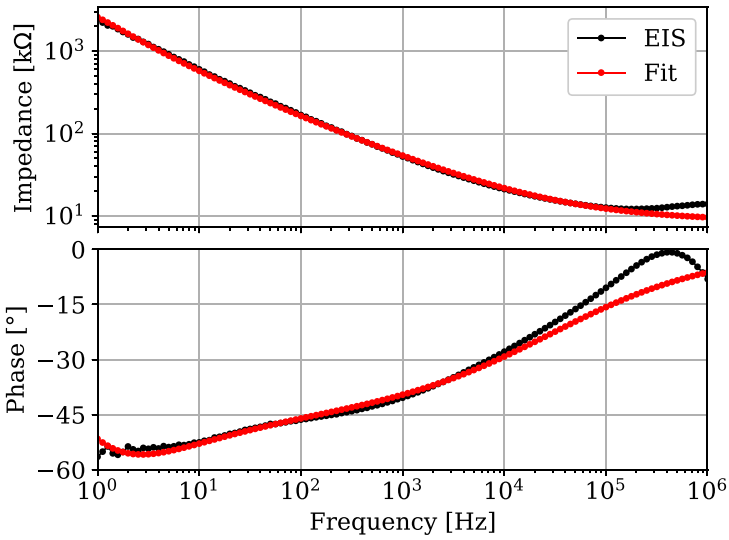

Figure 5. Bode plot of the impedance of the IrOx MEA between two selected electrode contacts. Electrochemical impedance spectroscopy (EIS) was conducted at room temperature and the spectra were fitted to the Randles circuit (5). At high frequencies above 10^5 Hz, the influence of parasitic impedances is visible, which are not accounted for in the equivalent circuit model.

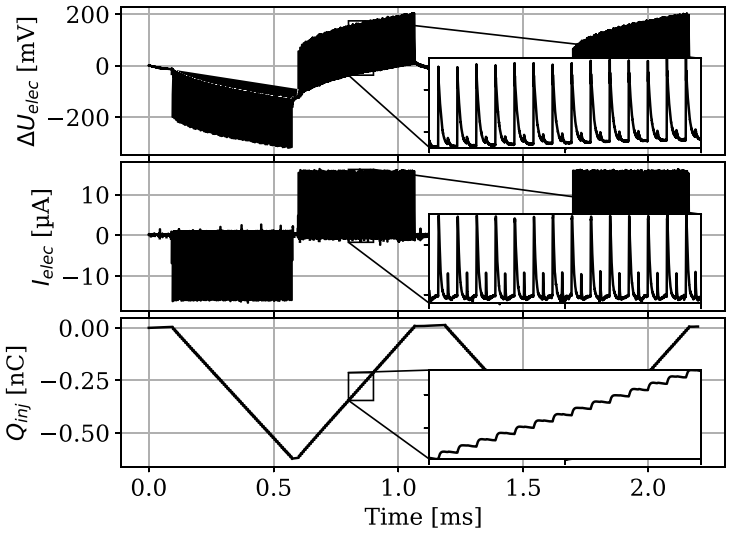

Figure 6. Transient measurement results of two stimulation periods with the IrOx electrodes in phosphate-buffered saline (PBS) solvent: (Top) measured difference electrode voltage ΔU_{elec}—(Middle) injected electrode current I_{elec}—(Bottom) injected charge quantity Q_{inj} @($T_{\mathrm{ph}} = 1$ ms, $n_{\mathrm{cat}} = n_{\mathrm{ano}} = 0.48$, $f_{\mathrm{mod}} = 140$ kHz, $\hat{U}_{\mathrm{mod}} = 800$ mV).

In total, the triangular shape of the injected charge amount stems from the rectangular stimulation waveform on the modulator voltage. During the interphase, the transferred charge is hold on the capacity of the ETI, where a discharge effect is available. This effect is caused by the polarisation effect of the IrOx electrodes [5]. After the anodic phase, a median residual charge amount of 5.32 pC ±2.6 pC remained. Compared to the injected charge amount of 1 nC, the relative rest charge to the injected charge amount was 0.482%. Also, the spikes had an effective time constant τ_{RC} of 207.64 ns, which allowed us to use a maximum modulator frequency $f_{\mathrm{mod,max}}$ of 481.6 kHz.

The stimulation allows to extract more information by analysing the charge transfer of each packet Q_{ph}, the effective double layer $C_{\mathrm{dl,eff}}$ and the effective tissue resistance $R_{\mathrm{tis,eff}}$ for each charge transfer cycle nT.

The calculation of Q_{ph} is done by integrating the electrical current and taking the difference between two cycles. The parameters of the simple Randles model were extracted by solving (7)

$$\Delta U_{\mathrm{elec}} = \frac{Q_{\mathrm{inj}} \cdot R_{\mathrm{tis}}}{T_{\mathrm{ph,cat}}} + \frac{Q_{\mathrm{inj}}}{C_{\mathrm{dl}}} \tag{7}$$

$$C_{\mathrm{dl}}(nT) = \frac{Q_{\mathrm{inj}}(nT) - Q_{\mathrm{inj}}((n-1)T)}{\Delta U_{\mathrm{elec}}(nT) - \Delta U_{\mathrm{elec}}((n-1)T)} \tag{8}$$

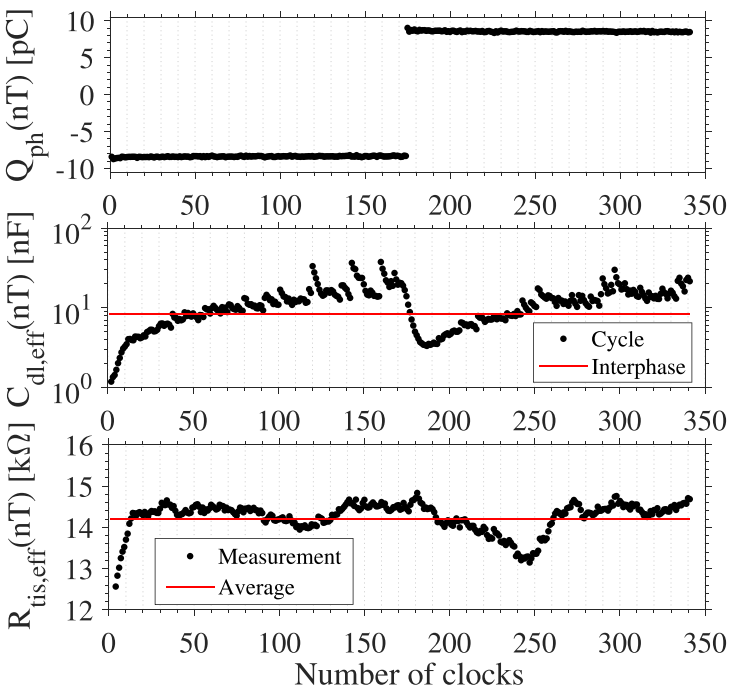

Figure 7. Transient measurement results of one stimulation phase with the IrOx electrodes in PBS solvent: (Top) injected charge quantity per phase—(Middle) effective double layer capacity—(Bottom) effective solvent resistance ($T_{\mathrm{ph}} = 1$ ms, $n_{\mathrm{cat}} = n_{\mathrm{ano}} = 0.48$, $f_{mod} = 140$ kHz, $\hat{U}_{\mathrm{mod}} = 800$ mV).

$$R_{\mathrm{tis}}(nT) = \frac{\mathrm{peak}\left(\Delta U_{\mathrm{elec}}(\tau)\right) - \Delta U_{\mathrm{elec}}\left((n-1)T\right)}{\mathrm{peak}\left(I_{\mathrm{elec}}(\tau)\right)}, \times \quad (n-1)T \leqslant \tau < nT. \tag{9}$$

C_{dl} is done after the complete charge transfer of each current pulse using (8) by considering the difference of the effective voltage change ΔU_{elec} and the transferred charge ΔQ_{inj}. Here, the impact of the resistive component is nearly zero due to the zero-current. $R_{\mathrm{tis,eff}}$ is extracted using (9) by looking at the peak of voltage drop and the peak of the charge current during the charge transfer in which the offset from the previous charge transfer is subtracted. In addition, an effective double layer capacity during the interphase was calculated using (7).

Figure 7 shows the extracted parameters from the measurement example (figure 6). The injected charge amount per cycle shows a constant behaviour in the cathodic and anodic phase of the stimulation in PBS (figure 7, top). During each phase, a charge package of 8.42 pC (±0.8%) in 168 cycles is generated and transferred to the interface.

The extracted value of the double layer capacity in figure 7(middle) shows a strongly charge-dependent capacity during stimulation which starts at 2.64 nF and ends at 10.72 nF in the end of the anodic phase. The same behaviour was observed during the anodic phase. During the interphase, an effective double layer capacity of 8.54 nF was estimated. The tissue resistance had a mean value of 14.18 kΩ, which was nearly constant over the stimulation duration. This non-linear behaviour of the double layer capacity is coming from the polarisation effect of the electrode material IrOx in PBS.

3.3. Comparison to EIS

We fitted the full Randles model to the impedance values obtained by EIS. Then, the parameters of the full Randles model were reduced to the simplified Randles model. This simplified model consists on a series connection of the double layer capacity (10) and tissue resistance (11)

$$C_{\mathrm{dl,Z}} = -\frac{1}{j\omega \cdot Im\{\underline{Z}_{\mathrm{elec}}\}} \tag{10}$$

$$R_{\mathrm{tis,Z}} = Re\{\underline{Z}_{\mathrm{elec}}\}. \tag{11}$$

These parameters were compared with the results obtained during the stimulation. In particular, the extracted double layer capacity during the interphase duration was considered. Figure 8 shows this comparison in which the stimulation period T_{stim} is sweeped. The shown frequency is extracted from the zeroth harmonic of the applied stimulation waveform and the corresponding frequency of the EIS are used.

The results indicate that the solution resistance determined from the stimulation is independent of the frequency and agrees with the parameter from the EIS with a maximum deviation of 8.25%. The capacity $C_{\mathrm{dl,eff}}$ decreases with increasing frequency, which can be explained by the inertia of the dipoles to the fast polarization orientation. At frequencies below 500 Hz, this is in agreement with the determined value from EIS with small variance. It represents the Helmholtz double-layer capacity and it shows

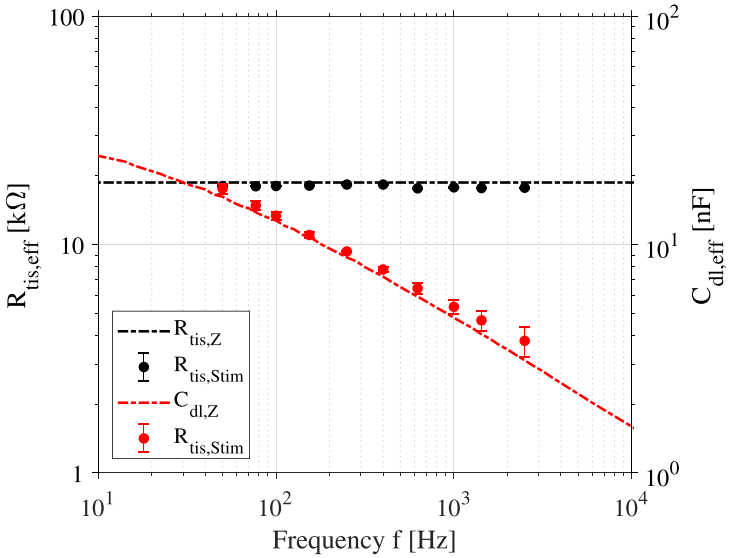

Figure 8. Measurement results of the effective double layer capacity $C_{dl,eff}$ and the effective solvent resistance $R_{tis,eff}$ as obtained by impedance spectroscopy (broken lines) and the biphasic stimulation using the charge controlled stimulation method.

that no electrochemical reactions are available. These results are caused by the properties of the electrode material [11] and not by the applied stimulation method.

This characteristic has an impact on the selection of the stimulation parameters and the safety of the stimulation during run-time, whereby a reduction in the effective double-layer capacity with increasing frequency causes a simultaneous reduction in the amount of charge that can be injected until electrolysis is triggered. This can lead to damage of the tissue and the electrode, which must be avoided for long-term operation. Also, it is recommended that a charge balancing technique should be applied with sensing the voltage differences at the stimulation front-end after stimulation due to the non-linearities of the metal-electrolyte interface tissue [26].

3.4. Broadband impedance fitting from electrical stimulation input

Next, we sought to explore if the transient signals of the performed electrical stimulation can be used to extract the parameters of the predicted Randles model during the applied stimulation. The general concept of our approach is shown in figure 9.

3.4.1. Model prediction

The first goal was to use the transient stimulation pulses to infer the parameters of the impedance model (5), which is frequency-dependent. For that, we Fourier transformed the transient pulses and estimated the impedance by dividing the voltage by the current spectrum (more details can be found in [42]). Then, we fitted the estimated impedance to (5) using ImpedanceFitter [40]. To check the obtained impedance estimate, we scaled the Fourier-transformed current with the estimated impedance based on the previous fit and applied the inverse Fourier transform. In this way, an estimate of the applied voltage is obtained, which can be directly compared with the measured stimulation voltage (figure 10). We observed that both the voltage obtained from the initial EIS characterization as well as from the impedance fitted from the stimulation pulses were in good agreement with the measured data. This indicates that assuming a linear model for the impedance is reasonable because strong nonlinear effects would cause a significant deviation of the expected and measured voltage [1]. Nevertheless, we had to apply an offset correction because the impedance model (5) diverges at frequencies tending to 0 Hz. For this reason, we set the impedance at 0 Hz to zero and instead matched the curves after applying the inverse Fourier transform. We expect non-linear electrochemical reactions to affect this offset because we could see that the global offset estimate had to be adjusted to exactly match a selection of the stimulation pulse (figure 10).

In our approach, the impedance is limited to the information contained in the frequency spectrum of the stimulation signal. Here, the minimally resolved frequency was usually about a few 100 Hz, which is considerably higher than the 1 Hz used in the EIS. For that reason, we checked if all parameters could be inferred. We accepted a parameter fit value if its uncertainty could be estimated by the fitting routine conducted in LMFIT and the estimated uncertainty was not extremely large. We chose an uncertainty limit of 10 times the fitted value because parameters that do not impact the fit result usually have uncertainties of more than 100 times the fitted value. When the fit error was too large or could not be inferred,

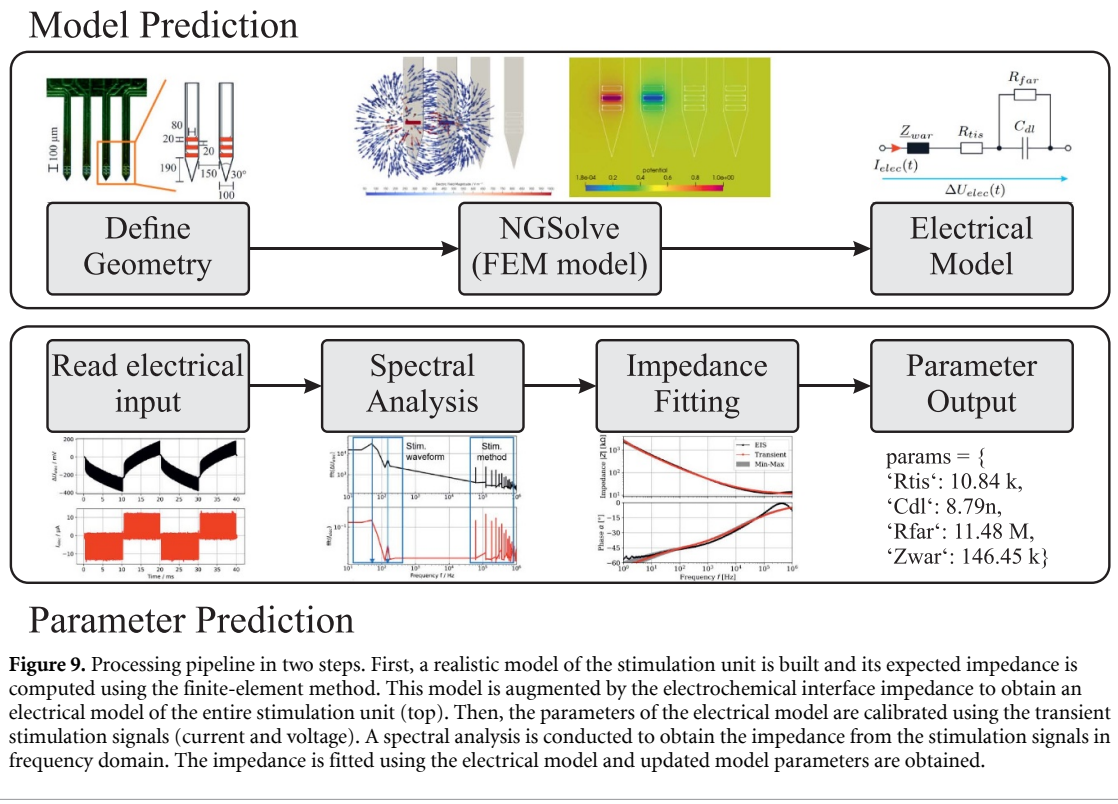

Figure 9. Processing pipeline in two steps. First, a realistic model of the stimulation unit is built and its expected impedance is computed using the finite-element method. This model is augmented by the electrochemical interface impedance to obtain an electrical model of the entire stimulation unit (top). Then, the parameters of the electrical model are calibrated using the transient stimulation signals (current and voltage). A spectral analysis is conducted to obtain the impedance from the stimulation signals in frequency domain. The impedance is fitted using the electrical model and updated model parameters are obtained.

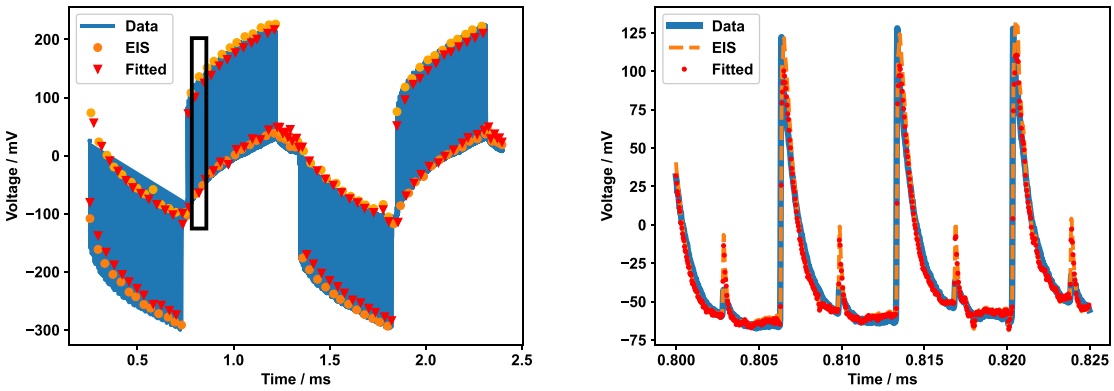

Figure 10. Comparison of the measured voltage (see figure 6) to voltages predicted from the initial EIS characterisation and the impedance model fitted to the stimulation pulses. For this example, an R_{tis} of 8.5 kΩ was fitted while the initial EIS characterisation yielded 9.9 kΩ. The Warburg coefficient was estimated to be 2.8 $\text{MΩ}/Hz^{-0.5}$ instead of 2.5 $\text{MΩ}/Hz^{-0.5}$. On the left, the envelope of the predicted voltages is shown together with the measured data. On the right, the full predicted signal is shown for a short stimulation period, which is indicated by the black box on the left. The impedance model diverges for frequencies tending to zero. Thus, an offset value of about 30 mV was fitted to match the predicted and measured curves. In the right panel, an additional offset of 35 mV was applied. For reference, the placed markers correspond to a sampling frequency of about 8 MHz.

we fixed parameter values to the value obtained in the EIS characterization. We found that the charge-transfer resistance could not be inferred for all tested waveforms. Importantly, fixing this parameter does not impair the prediction of the stimulation pulse (figure 10) because the shape of the stimulation pulse is not impacted by it. Similarly, the double-layer capacitance had little impact and was kept fixed for many waveforms. To not deteriorate the fit quality by parasitic impedances at high frequencies (see also figure 5), we imposed an upper frequency limit of 500 kHz. To further improve our approach, a model of the parasitic impedances should be added to (5). This could probably also improve the estimate of the tissue resistance, which appears to be slightly underestimated as indicated by the lower amplitude of the reconstructed stimulation pulses compared to the initial EIS estimate, which almost exactly matches the experimental data (figure 10).

To port the approach to the hardware level, we explored the dependency of the algorithm on the sampling frequency. A lower sampling frequency means fewer data points and is thus more hardware-friendly. We explored frequencies between 100 kHz

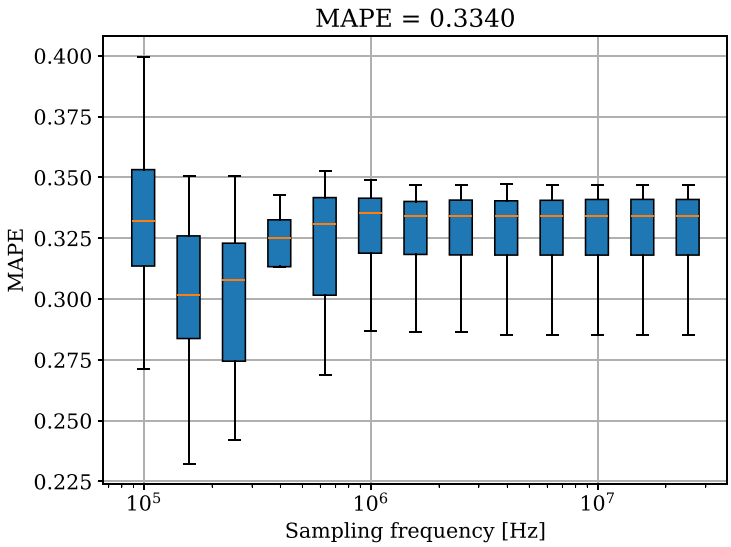

Figure 11. Extracted metric for mean absolute percentage error (MAPE) in dependency of the sampling frequency.

and 25 MHz, which corresponds to the original sampling rate. The lowest frequency yields a time step of 10 μs, which means that the overall signal is sampled but fine details are not resolved (compare also figure 10). We considered the mean absolute percentage error (MAPE) as a metric

$$\mathrm{MAPE} = \frac{1}{N}\sum_{k=1}^{N}\frac{|X[k]-Y[k]|}{|X[k]|}. \qquad (12)$$

Here, X is the electrical impedance from EIS, Y is the electrical impedance obtained from fitting the Fourier-transformed pulses, k is the index of the spectral frequency from EIS. MAPE is normalized with respect to the impedance magnitude so that a joint contribution of the whole impedance spectrum is considered. Hence, changes in the impedance magnitude do not impact the error metric.

Figure 11 shows the MAPE in dependency of the sampling rate using the electrical equivalent circuit in figure 1. With the original sampling rate of 25 MHz, a MAPE of 0.33 was obtained. The results suggest a sampling frequency beyond 1 MHz is necessary because the MAPE at lower frequencies has a higher variance and the mean MAPE value fluctuates significantly. At the frequencies below 1 MHz, the error comes from undersampling the stimulation signal as the sampling frequency approaches the modulator frequency of ChCS. Using lower sampling frequencies, the transient signal from stimulation transforms from the ChCS to a more smooth shape which is compatible with a more CCS.

The required sampling frequency is also reflected in the extracted parameter values of the full Randles model (figure 12). At high sampling frequencies above 1 MHz, consistent fitting values have been obtained. We found mean values for R_{tis} of 8.2 kΩ (±0.2 kΩ) and $\underline{Z}_{\mathrm{war}}$ of 2.80 MΩ/$Hz^{-0.5}$ (±0.15) for the best configuration. Compared to the fitted parameters of the initial characterization (section 2.2), the parameter deviations amounted to a ΔR_{tis} of 1.7 kΩ (17%) and a $\Delta\underline{Z}_{\mathrm{war}}$ of 0.3 MΩ/$Hz^{-0.5}$ (12%). Note that the EIS measurement was conducted before the stimulation sweeps and temperature fluctuations might have caused slight variations in the PBS conductivity. Depending on the required accuracy, also smaller sampling frequencies of, for example, 500 kHz could be used. For each application-specific stimulation waveform and impedance model, the presented analysis can be straightforwardly repeated to optimise the hardware settings. The main limitation is that the stimulation signal should cover a broad frequency range, which is in addition to the application for retina stimulation presented here, for example, also the case for conventional DBS stimulation pulses [42].

With the results of the parameter sweep of MAPE in figure 11 and of the electrical properties in figure 12, the uncertaincy increases at sampling rates lower than 1 MHz. The reason is, that the resampling of the data changes the properties of the transient signal. In figure 13, the manipulated transient stimulation signal is shown in which the sampling rate is changed from 25 MHz (from original data, see figure 6) to 1 MHz (left) and 140 kHz (right). Here, with decreased sampling rate f_s, the transient characteristic of the high-density ChCS is transformed into a CCS in which only the peaks are visible. In both cases, the applied charge injection is constant.

3.4.2. Digital twin formalism

After having established an electrochemical model of the stimulation electrodes and means to update the model *in situ*, we want to demonstrate how this information can be integrated with numerical modelling. For that, we first investigated the agreement

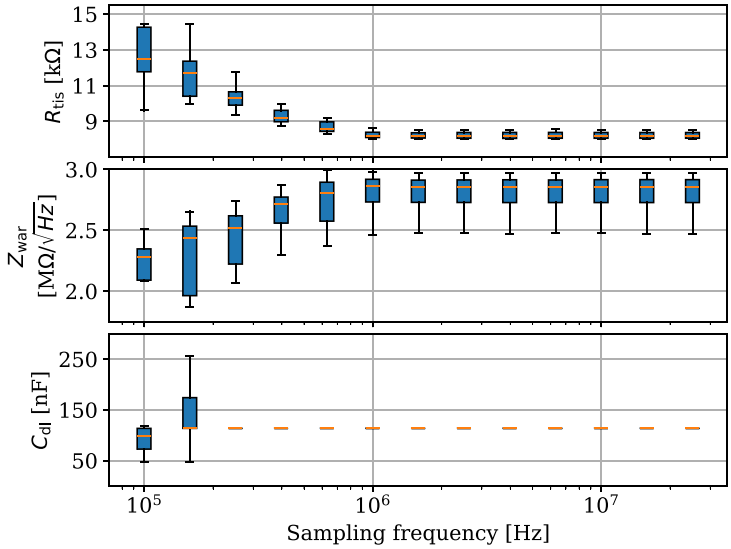

Figure 12. Electrical parameters of the used Randles model in dependency of the sampling frequency: (i) tissue resistance—(ii) Warburg impedance—(iii) double layer capacity (please note that a low variability in the box plot indicates that the value was fixed in the automated fitting routine).

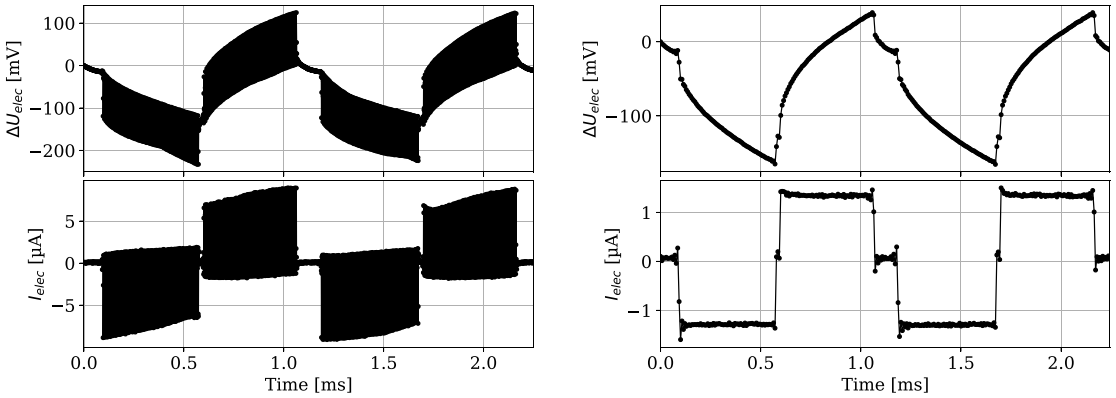

Figure 13. Manipulated transient measurement results of figure 6 with changing the sampling rate f_s: (Left) $f_s = 1$ MHz—(Right) $f_s = 140$ kHz.

between a numerical model and the experimental results.

First, we estimated the unit resistance of the electrode to be about 16.7 kΩ (i.e. at 1 S m^{-1}). The PBS buffer has a conductivity between 1.5 S m^{-1} and 2.0 S m^{-1} at room temperature. Thus, the expected measured resistance should roughly lie between 8.35 kΩ and 11.13 kΩ. This value was in good agreement with the measured value.

As a result, the electric field distribution can be reliably computed around the electrodes (see figure 9 top). The electrochemical interface impedance can be straightforwardly integrated and thus updated during the stimulation [41, 42]. In turn, the local stimulation pulse can be predicted by the numerical simulation. Hence, a local understanding of the stimulation is feasible with relatively high accuracy because the stimulation signal can be sufficiently well described by a linear model. Nevertheless, long-term investigations of the electrochemical interface and potential non-linear effects should be conducted to refine the model [3, 22].

Another possibility that arises from the numerical model is to estimate the induced voltage on the passive contacts. With that, it can be possible to estimate the electric field from measurements [41]. When we applied a voltage of 1 V to the centre contact of the first electrode and 0 V to the centre contact of the second electrode, the induced voltage on the other two contacts of the first electrode was numerically estimated to be 0.62 V. On the second electrode, a voltage of 0.38 V was induced, while the other contacts were all at 0.49 V in the numerical simulations. This suggests that the electric field can probably not be reliably estimated as there are only two usable data points at the active electrodes. However, the predicted symmetry around the center contact can be tested *in situ* and the voltage readouts can be used to test

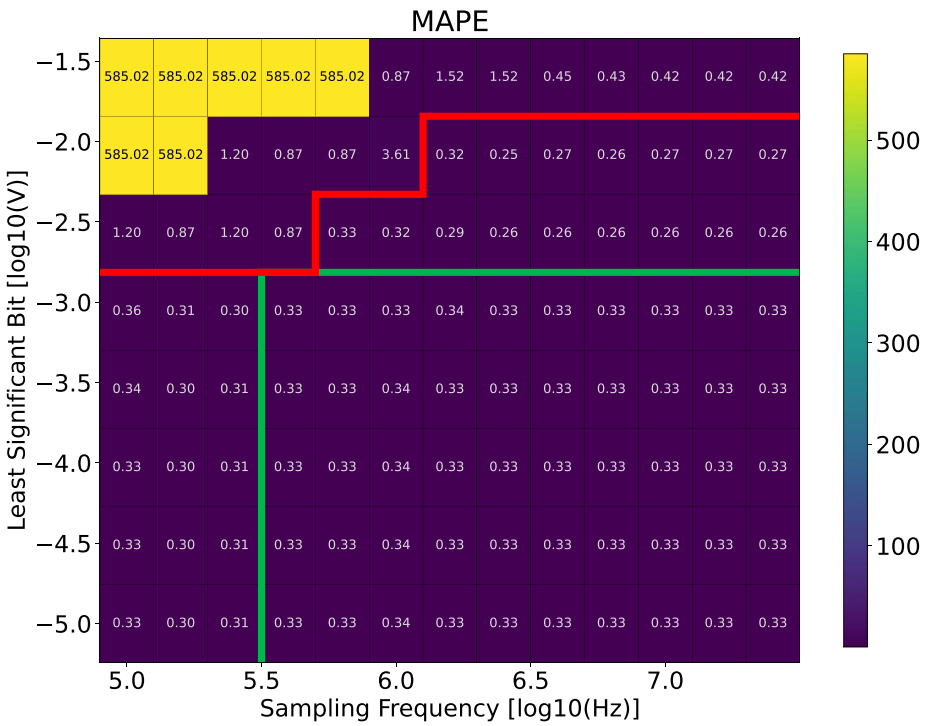

Figure 14. Result of the 2D parameter sweep by changing the sampling frequency and quantization level of the analog–digital converter for determining the mean absolute percentage error (MAPE). The LSB voltages was swept logarithmically from 10 μV to 25.4 mV. No signal reconstruction was feasible at high voltages (yellow squares), which is indicated by a high MAPE. At other configurations, relatively elevated MAPE values were obtained. Acceptable confiurations are separated by a red line (compare also figure 11). Optimal configurations are indicated by the green line.

if the stimulation electrode is functional. Thus, it is a measure to corroborate the results from the estimated impedance.

An additional perspective is to integrate the presented approach with electrochemical monitoring [6]. Our approach currently only measures the impact of electrochemical processes such as charge transfer, corrosion and pH changes on the impedance [7]. Other approaches can give more insight into the electrochemical nature of the processes and could be integrated into our workflow. However, to our knowledge, validating electrode geometries with numerical simulations is currently only possible with the approach presented in this work.

3.4.3. Analysis for using in embedded hardware.
To enable a real-time suitable execution of the signal processing pipeline for predicting the electrical parameters on the on-body electronic with an embedded system like a field programmable gate array or a microcontroller, a more detailed analysis is necessary. Here, we conducted an additional analysis of the analog–digital converter (ADC) parameters by sweeping the sampling rate f_s and the quantization level with the voltage value of the least significant bit U_{LSB}. This directly impacts further signal processing stages because less computational resources are available on embedded hardware compared to workstations.

As in the previous section, a MAPE of 0.33 was obtained at high sampling rates with high quantization levels, which drastically increased with decreased sampling rate and decreased quantization (figure 14). Specially for using this approach in ChCS, it is recommended to use sampling frequencies higher than 1 MHz and a LSB voltage lower than 3.16 mV, which represents a 10-bit successive-approximation ADC at a reference voltage of 2.5 V. If higher sampling rates and higher bit-resolution are required, it is recommended to use Pipeline-ADCs, which achieve 4 GHz at 14-bit [37] for high-speed applications or 260 MHz at 13-bit [39] for power-efficient applications. For the use in neural implants with limited chip area, it is recommended to avoid additional circuitry if a recording front-end is still available. Here, the reference voltage during stimulation can be increased in order to apply a higher voltage range of the ADC.

The presented approach can serve as a tool for tracking the changes in electrical impedance during long-term stimulation. This enables new characterization strategies in which (i) neurons and cells of interest can be identified by changes in the tissue impedance or (ii) the status of the microelectrode array and the tissue due to encapsulation effects can be diagnosed during run-time. For implementing the parameter prediction processing pipeline in hardware, optimizations of the used algorithms

are necessary in future. For example, the Fourier transformation could be replaced by wavelet transformation. This would reduce the memory requirements and the computational effort.

4. Conclusion

We presented two approaches for predicting the electrical parameters of the stimulation path in neurostimulation applications by processing the transient signals of the electrical stimulation. These approaches have been tested in PBS by performing the ChCS method with microelectrode arrays designed for layer-selective stimulation of retinal structures.

In the first approach, the parameters of the double-layer capacity and the tissue resistance are extracted by sensing the voltage responses due to the ChCS. This enables extracting the non-linearity properties of the metal-electrolyte interface during the stimulation in order to identify polarisation effects. Also, it allows defining design rules for neural stimulation front-ends in which the non-linearity must be considered in the design phase, in which the maximum injectable charge quantity depends on the applied phase duration. In addition, it is recommended to employ the charge balancing technique based on sensing the voltage after each stimulation.

In the second approach, the electrical impedance is fitted based on the Fourier transformation of the transient signals (current and voltage) during stimulation. From this, the electrical parameters of the full Randles model are extracted. Compared to the first approach, long-term changes in electrical impedance can be determined with an accuracy of 10%–20%. Moreover, the stimulation pulse can be predicted and hence the validity of the applied impedance model can be straightforwardly assessed. Together with the validated numerical model, this approach can be used to realise a digital twin and provide a local understanding of electrical stimulation for various applications such as retina stimulation or DBS.

Data availability statement

The data and code that support the findings of this study are openly available at the following URL/DOI: https://doi.org/10.5281/zenodo.15064621.

Acknowledgments

Parts of this work were funded by the *Deutsche Forschungsgemeinschaft* (DFG, German Research Foundation), Projects 143692466, 424556709, and SFB 1270/1,2—299150580. Microfabrication was carried out in the Central Laboratory of Micro- and Nanotechnology (ZMNT) at RWTH Aachen University. We acknowledge support by the Open Access Publication Fund of the University of Duisburg-Essen.

ORCID iDs

Andreas Erbslöh https://orcid.org/0000-0001-6702-892X
Julius Zimmermann https://orcid.org/0000-0003-1486-0426
Sven Ingebrandt https://orcid.org/0000-0002-0405-2727
Karsten Seidl https://orcid.org/0000-0001-6197-5037
Ursula van Rienen https://orcid.org/0000-0003-1042-2058
Gregor Schiele https://orcid.org/0000-0003-4266-4828
Rainer Kokozinski https://orcid.org/0000-0003-3416-3310

References

[1] Bielfeldt M *et al* 2023 Discrimination between the effects of pulsed electrical stimulation and electrochemically conditioned medium on human osteoblasts *J. Biol. Eng.* **17** 71
[2] Boehler C, Carli S, Fadiga L, Stieglitz T and Asplund M 2020 Tutorial: Guidelines for standardized performance tests for electrodes intended for neural interfaces and bioelectronics *Nat. Protoc.* **15** 3557–78
[3] Cantrell D R, Inayat S, Taflove A, Ruoff R S and Troy J B 2008 Incorporation of the electrode-electrolyte interface into finite-element models of metal microelectrodes *J. Neural Eng.* **5** 54–67
[4] Carlyon R and Goehring T 2021 Cochlear implant research and development in the twenty-first century: a critical update *J. Assoc. Res. Otolaryngol.* **22** 481–508
[5] Cogan S F 2008 Neural stimulation and recording electrodes *Annu. Rev. Biomed. Eng.* **10** 275–309
[6] Doering M, Kieninger J, Kübler J, Hofmann U G, Rupitsch S J, Urban G A and Weltin A 2023 Advanced electrochemical potential monitoring for improved understanding of electrical neurostimulation protocols *J. Neural Eng.* **20** 036036
[7] Ehlich J, Migliaccio L, Sahalianov I, Nikić M, Brodský J, Gablech I, Vu X T, Ingebrandt S and Głowacki E D 2022 Direct measurement of oxygen reduction reactions at neurostimulation electrodes *J. Neural Eng.* **19** 036045
[8] Erbslöh A, Viga R, Walter P, Kokozinski R and Grabmaier A 2017 Implementation of a charge-controlled stimulation method in a monolithic integrated CMOS-chip for excitation of retinal neuron cells *2017 Austrochip Workshop on Microelectronics (Austrochip)* pp 47–52
[9] Erbslöh A, Buron L, Ur-Rehman Z, Musall S, Hrycak C, Löhler P, Klaes C, Seidl K and Schiele G 2024 Technical survey of end-to-end signal processing in BCIs using invasive MEAs *J. Neural Eng.* **21** 051003
[10] Fan B, Wolfrum B and Robinson J T 2021 Impedance scaling for gold and platinum microelectrodes *J. Neural Eng.* **18** 056025
[11] Fang X, Wills J, Granacki J, LaCoss J, Arakelian A and Weiland J 2007 Novel charge-metering stimulus amplifier for biomimetic implantable prosthesis *2007 IEEE Int. Symp. on Circuits and Systems (ISCAS)* pp 569–72
[12] Frey J, Cagle J, Johnson K A, Wong J K, Hilliard J D, Butson C R, Okun M S and de Hemptinne C 2022 Past, present and future of deep brain stimulation: hardware, software, imaging, physiology and novel approaches *Front. Neurol.* **13** 825178
[13] Hejazi M, Tong W, Ibbotson M R, Prawer S and Garrett D J 2021 Advances in carbon-based microfiber electrodes for neural interfacing *Front. Neurosci.* **15** 658703

[14] Hsu W-Y and Schmid A 2017 Compact, energy-efficient high-frequency switched capacitor neural stimulator with active charge balancing *IEEE Trans. Biomed. Circuits Syst.* **11** 878–88
[15] Im M and Kim S 2020 Neurophysiological and medical considerations for better performing microelectronic retinal prothesis *J. Neural Eng.* **17** 1–9
[16] Kauth A, Mildner A-K, Hegel L, Wegener J and Ingebrandt S 2024 Development of specialized microelectrode arrays with local electroporation functionality *Ann. Biomed. Eng.* **52** 12–21
[17] Lee H-M, Kwon K Y, Li W and Ghovanloo M 2015 A power-efficient switched-capacitor stimulating system for electrical/optical deep brain stimulation *IEEE J. Solid-State Circuits* **50** 360–74
[18] Lempka S F, Miocinovic S, Johnson M D, Vitek J L and McIntyre C C 2009 *In vivo* impedance spectroscopy of deep brain stimulation electrodes *J. Neural Eng.* **6** 046001
[19] Lewis C M, Boehler C, Liljemalm R, Fries P, Stieglitz T and Asplund M 2024 Recording quality is systematically related to electrode impedance *Adv. Healthcare Mater.* **13** 2303401
[20] Lorach H *et al* 2023 Walking naturally after spinal cord injury using a brain–spine interface *Nature* **618** 126–33
[21] Negi S, Bhandari R, Rieth L, Van Wagenen R and Solzbacher F 2010 Neural electrode degradation from continuous electrical stimulation: comparison of sputtered and activated iridium oxide *J. Neurosci. Methods* **186** 8–17
[22] Opancar A, Glowacki E D and Derek V 2024 Choosing the right electrode representation for modeling real bioelectronic interfaces: a comprehensive guide *J. Neural Eng.* **21** 046049
[23] Prasad A, Xue Q-S, Sankar V, Nishida T, Shaw G, Streit W J and Sanchez J C 2012 Comprehensive characterization and failure modes of tungsten microwire arrays in chronic neural implants *J. Neural Eng.* **9** 056015
[24] Parmeggiani F, Sorrentino F S, Ponzin D, Barbaro V, Ferrari S and Di Iorio E 2011 Retinitis pigmentosa: genes and disease mechanisms *Curr. Genomics* **12** 238–49
[25] Ramasubbu R, Lang S and Kiss Z H T 2018 Dosing of electrical parameters in deep brain stimulation (DBS) for intractable depression: a review of clinical studies *Front. Psychiatry* **9** 302
[26] Richardot A and McAdams E 2002 Harmonic analysis of low-frequency bioelectrode behavior *IEEE Trans. Med. Imaging* **21** 604–12
[27] Rincón Montes V, Gehlen J, Lück S, Mokwa W, Müller F, Walter P and Offenhäusser A 2019 Toward a bidirectional communication between retinal cells and a prosthetic device—a proof of concept *Front. Neurosci.* **13** 367
[28] Sandoval-Pistorius S S, Hacker M L, Waters A C, Wang J, Provenza N R, de Hemptinne C, Johnson K A, Morrison M A and Cernera S 2023 Advances in deep brain stimulation: from mechanisms to applications *J. Neurosci.* **43** 7575–86
[29] Sankar V, Patrick E, Dieme R, Sanchez J C, Prasad A and Nishida T 2014 Electrode impedance analysis of chronic tungsten microwire neural implants: understanding abiotic vs. biotic contributions *Front. Neuroeng.* **7** 13
[30] Schöberl J 2014 C++ 11 implementation of finite elements in NGSolve *Technical Report* ASC-2014-30 (Institute for Analysis and Scientific Computing)
[31] Schöberl J 1997 NETGEN an advancing front 2D/3D-mesh generator based on abstract rules *Comput. Vis. Sci.* **1** 41–52
[32] Shah N P, Madugula S, Grosberg L, Mena G, Tandon P, Hottowy P, Sher A, Litke A, Mitra S, Chichilnisky E 2019 Optimization of electrical stimulation for a high-fidelity artificial retina *2019 9th Int. IEEE/EMBS Conf. on Neural Engineering (NER)* pp 714–8 (https://doi.org/10.1109/NER.2019.8716987)
[33] Shepherd R K, Carter P M, Dalrymple A N, Enke Y L, Wise A K, Nguyen T, Firth J, Thompson A and Fallon J B 2021 Platinum dissolution and tissue response following long-term electrical stimulation at high charge densities *J. Neural Eng.* **18** 036021
[34] Simpson J and Ghovanloo M 2007 An experimental study of voltage, current and charge controlled stimulation front-end circuitry *2007 IEEE Int. Symp. on Circuits and Systems (ISCAS)* pp 325–8
[35] Steinmetz N A *et al* 2021 Neuropixels 2.0: a miniaturized high-density probe for stable, long-term brain recordings *Science* **372** eabf4588
[36] Wang C, Brunton E, Haghgooie S, Cassells K, Lowery A and Rajan R 2013 Characteristics of electrode impedance and stimulation efficacy of a chronic cortical implant using novel annulus electrodes in rat motor cortex *J. Neural Eng.* **10** 046010
[37] Yang P, Li F and Wang Z 2024 A 14-bit 4 GS/s two-way interleaved pipelined ADC with aperture error tunning *IEEE Trans. Circuits Syst.* II **71** 2961–5
[38] Zheng X S, Tan C, Castagnola E and Cui X T 2021 Electrode materials for chronic electrical microstimulation *Adv. Healthcare Mater.* **10** 2100119
[39] Zhou D, Briseno-Vidrios C, Jiang J, Park C, Liu Q, Soenen E G, Kinyua M and Silva-Martinez J 2019 A 13-bit 260MS/s power-efficient pipeline ADC using a current-reuse technique and interstage gain and nonlinearity errors calibration *IEEE Trans. Circuits Syst.* I **66** 3373–83
[40] Zimmermann J and Thiele L 2021 j-zimmermann/ImpedanceFitter: v2.0.2 *Zenodo* https://doi.org/10.5281/zenodo.5116618
[41] Zimmermann J, Sahm F, Arbeiter N, Bathel H, Song Z, Bader R, Jonitz-Heincke A and van Rienen U 2023 Experimental and numerical methods to ensure comprehensible and replicable alternating current electrical stimulation experiments *Bioelectrochemistry* **151** 108395
[42] Zimmermann J, Budde K, Arbeiter N, Molina F, Storch A, Uhrmacher A M and van Rienen U 2021 Using a digital twin of an electrical stimulation device to monitor and control the electrical stimulation of cells *in vitro Front. Bioeng. Biotechnol.* **9** 765516